Supporting information for

Electrodeposition-based in situ construction of a ZnO-ordered macroporous film gas sensor with enhanced sensitivity

Zizhao Pan[a], Fengqiang Sun[a, b, c], Ximiao Zhu[a], Zhicong Chen[a], Xi Lin[a], Yujian Zheng[a], Wenyu Zhong[a], Zefeng Zhuang[a] and Fenglong Gu[b]

[a] School of Chemistry and Environment, South China Normal University, Guangzhou 510006, PR China

[b] Key Laboratory of Theoretical Chemistry of Environment, Ministry of Education, South China Normal University, PR China

[c] Guangzhou Key Laboratory of Materials for Energy Conversion and Storage, PR China

---

S1. The increased surface area caused by the introduction of ordered spherical macroporous structure into a film

It is considered that the macroporous film has the same fine structure as the flat film on the same size substrate, so the increase in surface area is caused only by the macroporous structure. Since the macroporous film is formed by the induction of colloid crystal composed closely packed PS microsphers, the area of the flat film and the vertical projected area of the macroporous film both

should be $N\times\pi R^2$, where N and R represents the number and the radius of the template microspheres or the macropores, respectively (Fig. S1). Ideally, supposing both sides of a macropore can be exposed, the increased multiple (IM) in surface area can be calculate as Eq. 1S. The height (h) is less than 2R, and regardless of the macropore size, the IM will be less than 7.

$$IM = \frac{N\times 2\times 2\pi Rh - N\pi R^2}{N\pi R^2} = \frac{4h-R}{R} < 7 \qquad (1S)$$

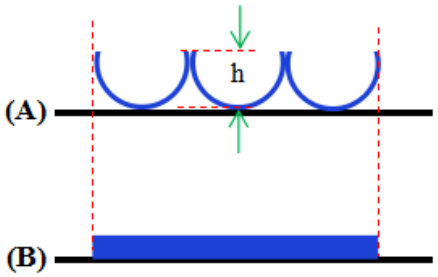

Fig. S1 Macroporous film (A) and flat film (B). The vertical projected area of the macroporous film is equal to the area of the flat film.

S2. The typical existence states of interstice space of macroporous film

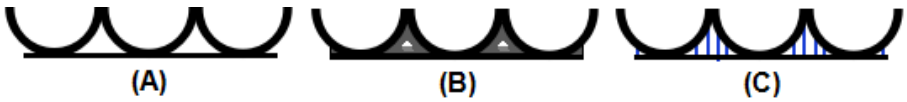

Fig. S2 Typical existence states of interstice space under macropore array: (A) empty; (B) almost completely filled and (C) specifically filled by a new designed structure.

S3. WS-30A gas-sensing test system and its operations

The whole test system (Fig. S3A) consists of a test instrument (left) and a computer system (right)

connected to it. The test instrument is placed into a ventilating closet to ensure environmental safety and rapid removal of detected gases. The details of the instrument are shown in the photo in Fig. S3B and the corresponding diagram in Fig. S3C. The test chamber, the fans, the evaporation table, the test board and the load resistor are marked, respectively. Besides, there is a hole in the test-chamber-wall near the evaporation table, and on the operation panel of the instrument, there are two knobs for regulating the voltage and two buttons for heating the evaporation table. The working voltage is the only parameter to be calibrated for this instrument, which is usually done before it leaves the factory. If necessary, the factory will send technicians to disassembly the instrument and calibrate it with a high-precision voltage calibrator. Therefore, in daily operation, we only need to set the working voltage and heating voltage, and select the appropriate load resistor. The working principle of this instrument has been explained in the text.

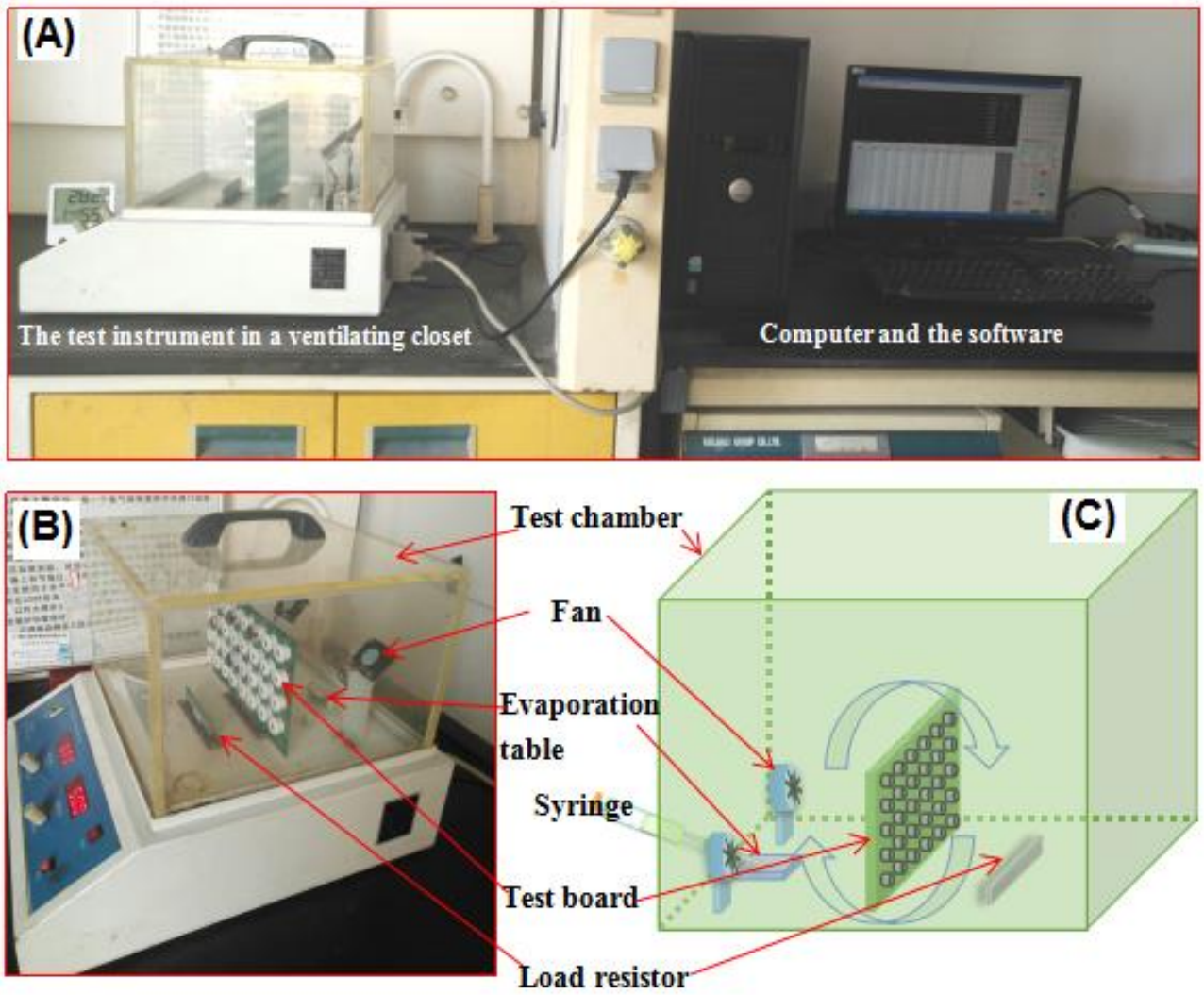

Fig. S3 WS-30A gas-sensing test system. (A) The digital photo of the system. (B) The photo of the test instrument. (C) A schematic diagram of the test instrument.

For the introduction of ethanol gas for detection, a calculated volume of liquid ethanol (99.9% purity) was extracted with a micro-syringe and then was dropped onto the evaporation table through the hole of the chamber, in the working state of the instrument. Subsequently, the heating button was immediately pressed to heat the evaporation platform so that ethanol evaporated quickly. With the aid of the fans the vapor could be quickly dispersed in the chamber. To achieve a certain concentration of ethanol gas, the amount of liquid ethanol that needed to be injected was calculated

according to Eq. S2:

$$V_{liquid} = \frac{(V_{chamber} \times 1000) \times (C_{gas} \times 10^{-6})}{\frac{\rho_{liquid} \times C_{liquid}}{M} \times 22.4 \times \frac{T_s}{298} \times 1000} \quad \text{(S2)}$$

where V_{liquid} is the volume of liquid ethanol to be injected (μL), $V_{chamber}$ is the total volume of the chamber (18 L), C_{gas} is the concentration of ethanol gas (ppm), M is the molecular weight of ethanol gas, T_s is the surrounding temperature (K), ρ_{liquid} is the density of liquid ethanol (g/cm^3) and C_{liquid} is the weight concentration of liquid ethanol (%). Other VOC gases could be injected into the chamber by this way.

S4. XRD patterns of electrodeposited samples and MS-ZnO-10 film with log(I) coordinates

Fig. S4 shows the patterns. It can be found that, comparing with the patterns with I coordinates, these patterns can display as many crystal diffraction peaks as possible. For instance, in the pattern of the sample from 5 min of ED, the peaks corresponding to Zn(002) and Zn(100) planes can be clearly observed. Except for the C(002) peak, there are only the peaks of Zn in all electrodeposited samples, and only the peaks of ZnO in MS-ZnO-10 film, which further confirms that the metallic Zn and ZnO are the only crystalline substance in the electrodeposition samples and in MS-ZnO-10 film, respectively. No impurity can be found.

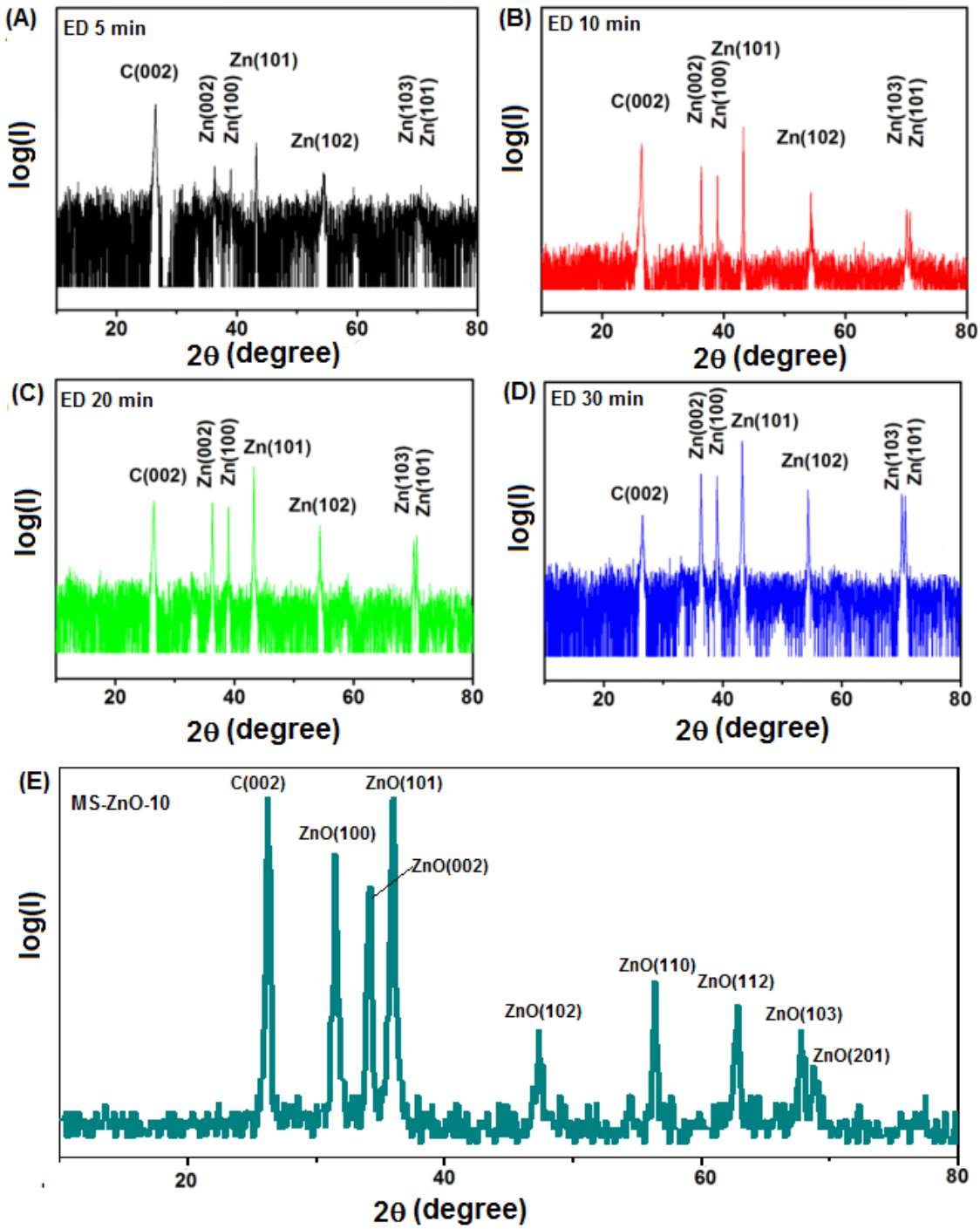

Fig. S4 XRD patterns of electrodeposited samples with ED time of 5 min (A), 10 min (min), 20 min (C) and 30 min (D). And XRD pattern of MS-ZnO-10 film (E). log (I), instead of I, is taken as the coordinate.

S5. TEM image of the Ed sample obtained by the electrodeposition induced by SDS only

Fig. S5A shows a nanosheet scraped from the ceramic tube. The SAED displays the typical single crystal state of the nanosheet and the diffraction dots corresponding Zn(100) and Zn(101) crystal planes can be determined (inset of Fig. S5A). Upon observation of the HRTEM (Fig. S5B), lattice fringes with distances of 0.23 nm and 0.21 nm corresponding to the two crystal planes of metallic Zn are also confirmed. This explains the metallic grow into nanosheets in the electrodepostion process, and correspondingly, the composition of fine particles, nano-patches and shells formed on PS microspheres in the template&SDS-iduced electrodeposition should be $Zn(OH)_2$.

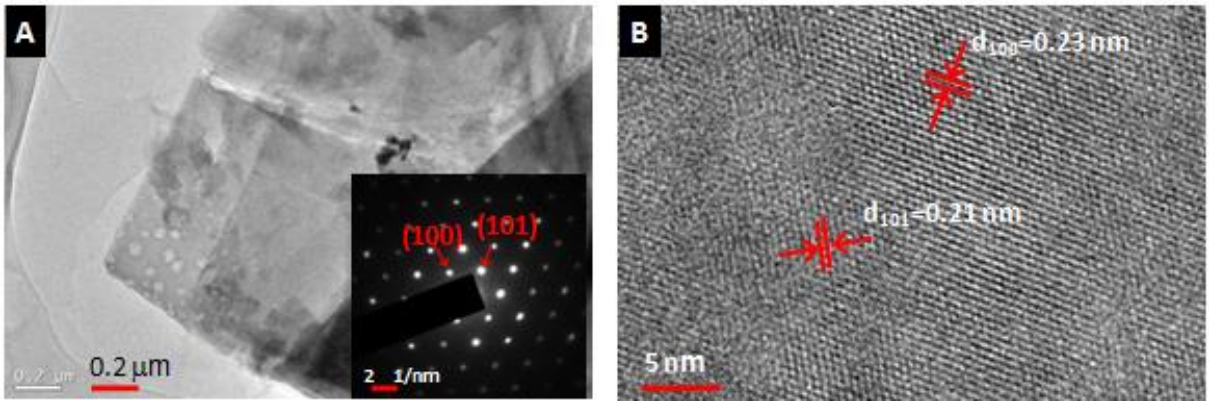

Fig. S5 TEM characterization of the Ed sample from the electrodeposition induced by SDS only. (A) A low magnification image; (B) HRTEM image. Inset of A shows an SEAD pattern.

S6. XRD patterns of Ed samples from different electrodeposition conditions

Fig. S6 shows XRD patterns of Ed samples derived from the electrodeposition free of template&SDS, induced by template only and induced by SDS only, respectively. All samples were electrodeposited 10 min. Metallic Zn always generates in the process, regardless of the electrodeposition conditions. Importantly, all samples have similar patterns and the relative intensity of peaks of different samples is almost constant, which explains that the crystallization habit of

metallic Zn is not affected by the template and SDS in the $ZnSO_4$ solution. Since metallic Zn easily grow into nanosheet in the pure $ZnSO_4$ solution according to the crystallization habit (as shown in Fig. 4A), Zn nanosheets should also generate in SDS or template added $ZnSO_4$ solution. SDS or template can only change the growth mode of nanosheets by physical restriction, thus inducing different morphologies of nanosheets (as shown in Fig.s 4B and C, and Fig. 2). All Ed samples can be transformed into ZnO films after the heat-treatment and have similar XRD patterns (as shown in Fig. 3C).

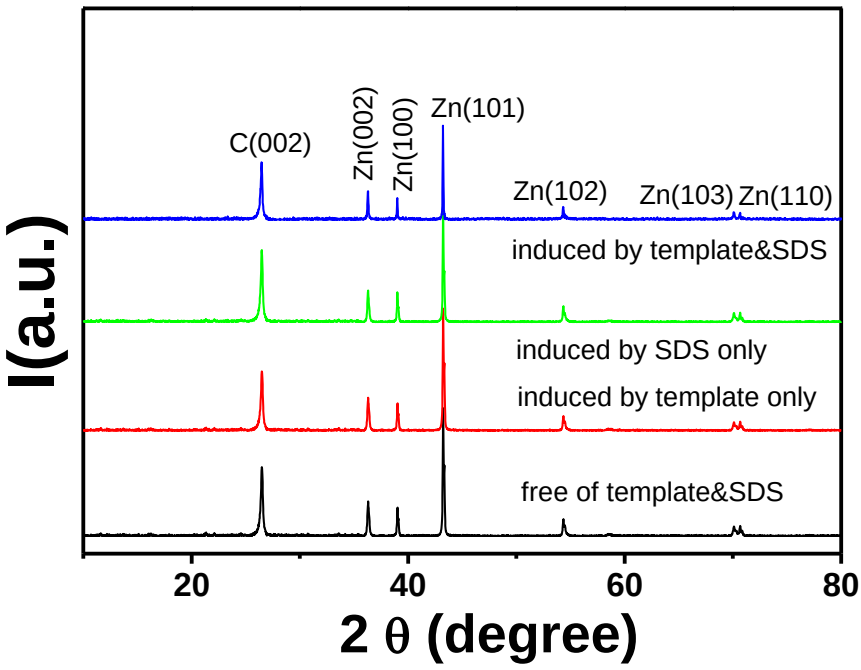

Fig. S6 XRD patterns of Ed samples from different electrodeposition conditions

S7. Change of graphite coating auxiliary conductive layer

For any electrodeposited sample, the morphology and the conductivity of the auxiliary conductive layer (i. e. the graphite coating) on the ceramic tube could be simultaneously changed in

the process of converting Zn to ZnO by heating, as shown in Fig. S7. Fig. S7A shows the initial graphite coating before electrodeposition, which is dense and almost without defects. Naturally, it has high conductivity and shows a resitance of ~80 Ω. Fig. S7B displays a final graphite coating after dissolution removal of ZnO film on it by HCl solution. It had experienced the electrodeposition and the heat-treament processes. Obviously, comparing to the original dense graphite coating, the morphology was changed a lot. The fine carbon particles and the edge of graphite sheets were removed by oxidation in the heat-treatment process and only fragmentary graphite sheets distributed disorderly on the ceramic tube. At the same time, the graphite sheets could generate inconsistent expansion and shrinkage due to their different sizes, which led to the separation of adjacent sheets and the generation of large defects or cracks. As a result, as we measured, the conductivity of such graphite coating had been completely eliminated. It should be mentioned, the variation of the graphite coating for all heated samples was almost consistent and the variation couldn't lead to the generation of cracks on the ZnO film due to the buffer action of the Zn or ZnO nanosheets. At the same time, ZnO films could be well in-situ sintered onto surfaces of the ceramic tube and the residual graphite sheets, and thereby had high stability. The residual graphite sheets, like conductive wires, could make the ZnO films had better conductivity. ZnO films on such non-conductive surface could surely act as the role of the sensing film of the resistive-type gas-sensor.

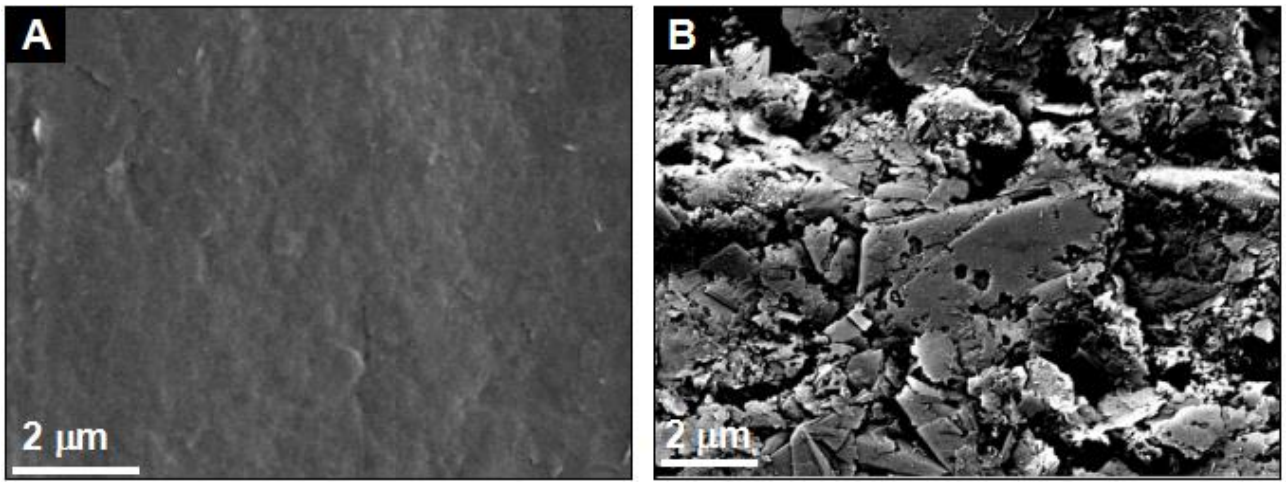

Fig. S7 The initial graphite coating before electrodeposition (A) and the final graphite coating after experiencing the electrodeposition and the heat-treatment (B). For observing the real final graphite coating, the ZnO film on it was dissolved and removed with HCl solution.

S8. Variations of resistance and sensing response of the sensor with heating time in the heat treatment process

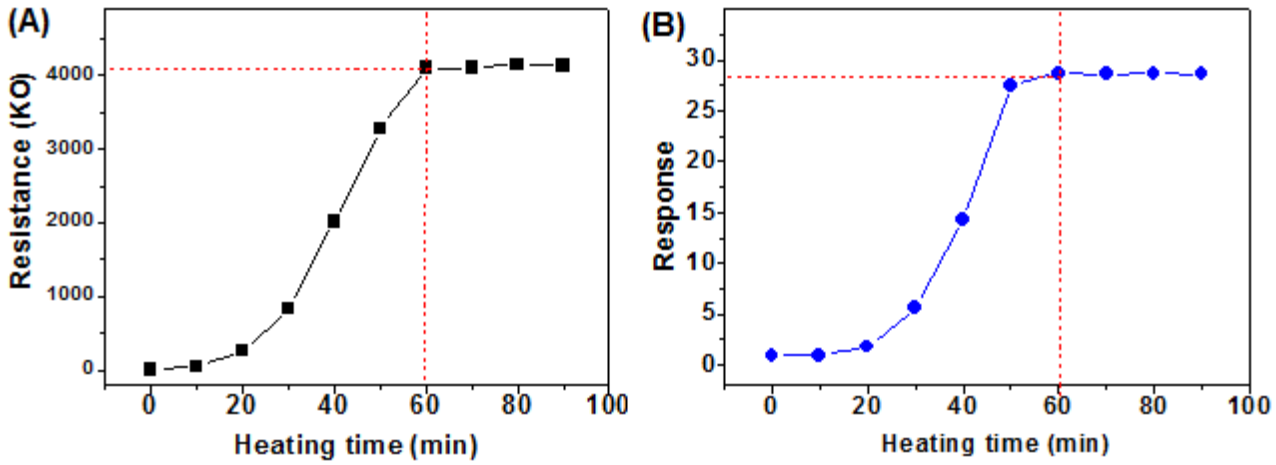

Fig. S8 Variations of resistance (A) and sensing response (B) of MS-ZnO-10 sensor with heating time in the heat treatment process. The concentration of the ethanol gas was 50 ppm.

S9. Analysis on O 1s XPS spectra of MS-ZnO-10 film

As shown in Fig. S9, the O1s XPS peak of MS-ZnO-10 film can be separated into three main components after Gaussian fitting. The peak centered at 530.08 eV (O_L) is attributed to O^{2-} ions in the ZnO crystal, the peak centered at 531.18 eV (O_V) is associated with O^{2-} ions in oxygen-deficient regions within the matrix of ZnO , while the peak centered at 531.98 eV (O_C) is usually attributed to chemisorbed and dissociated oxygen species.[1-3] The chemisorbed and dissociated oxygen species will react with the ethanol gas when the film acts as the sensing film of a sensor.

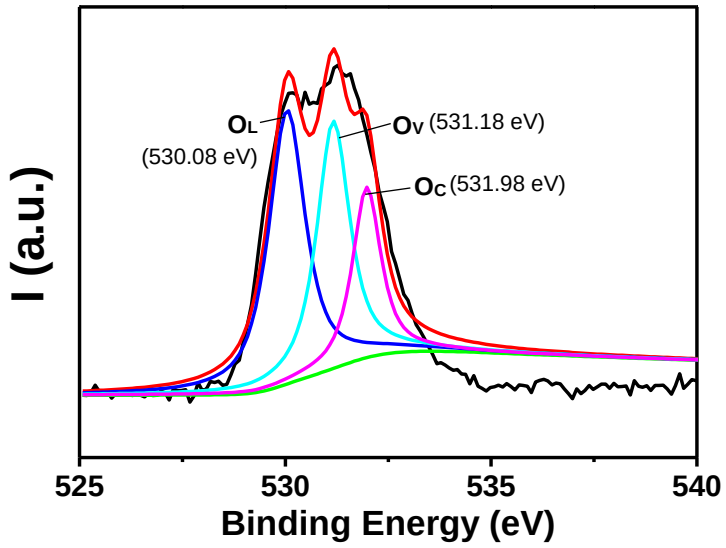

Fig. S9 The O 1s XPS spectra of MS-ZnO-10 film

S10. Sensing responses of the MS-ZnO films derived from different ED time

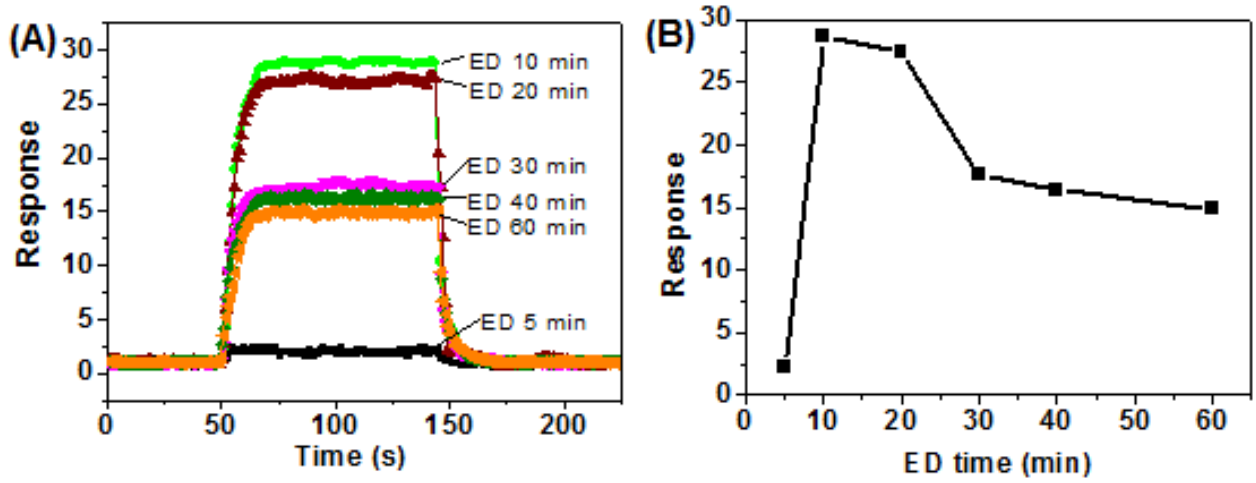

Fig. S10 (A) Dynamic responses of MS-ZnO serial films derived from different ED time. (B) A summary on the variation of the response of the films with ED time. The concentration of the ethanol gas was 50 ppm.

S11. Comparison of sensing performance between MS-ZnO-10 thin film sensor and other conventional material sensors

Table S1 Comparison of sensing performances of various ethanol gas sensors

Materials	Working Temperature (℃)	Sensitivity/ Concentration (ppm)	Response time/ Recovery time (s)	Ref
SnO_2 nanofibers	330	18/ 200	13/ 13.9	4
TiO_2 nanobelts	400	8/ 50	-/-	5
In_2O_3 nanowires	370	2/ 100	10/ 20	6
WO_3 thick films	400	14.2/ 50	10/ 45s	7
α-Fe_2O_3 nanoparticles	225	10/ 100	5/ 600	8
CuO nanowires	240	1.5/ 1000	110/ 120	9
Thin-walled NiO tubes	400	1.69/ 100	-/-	10
Hollow Co_3O_4 microspheres	180	16/ 100	6/ 22	11
$ZnCo_2O_4$ nanosheet	400	4/ 100	-/-	12
Hierarchical $ZnSnO_3$ Nanocages	270	10/ 50	-/-	13
CuO/ZnO/g-C_3N_4 ternary composite	260	16/ 500	87/ 169	14
Branch-like NiO/ZnO heterostructures	400	6.7/ 50	>240/ >240s	15
Spongy MoO_3 hierarchical nanostructures	250	19.8/ 100	15/ 15s	16
MS-ZnO-10 film	200	28.7/ 50	13/ 8	This work

S12. Generality of electrodeposition-based method in construction of semiconductor film sensor with specific structure

The electrodeposition method provides a general and promising route in in-situ construction of various semiconductor gas sensor with a specific structure and the enhanced sensing performances. For example, still taking the two-dimensional colloid crystal as the template and according to the strategy shown as Scheme 1, we has also realized the construction of a SnO_2 hollow microsphere film gas sensor and a CuO ordered macroporous film gas sensor (Fig. S11). Both of them exhibit considerably enhanced sensing response to ethanol gas, compared with the ordinary film electrodeposited without the assistance of template or surfactant. Actually, in addition to ZnO, SnO_2

and CuO, many other micro/nano-structured semiconductor film sensors have been designed to be constructed with the aid of template and/or surfactant, showing good expectations and are being systematically studied.

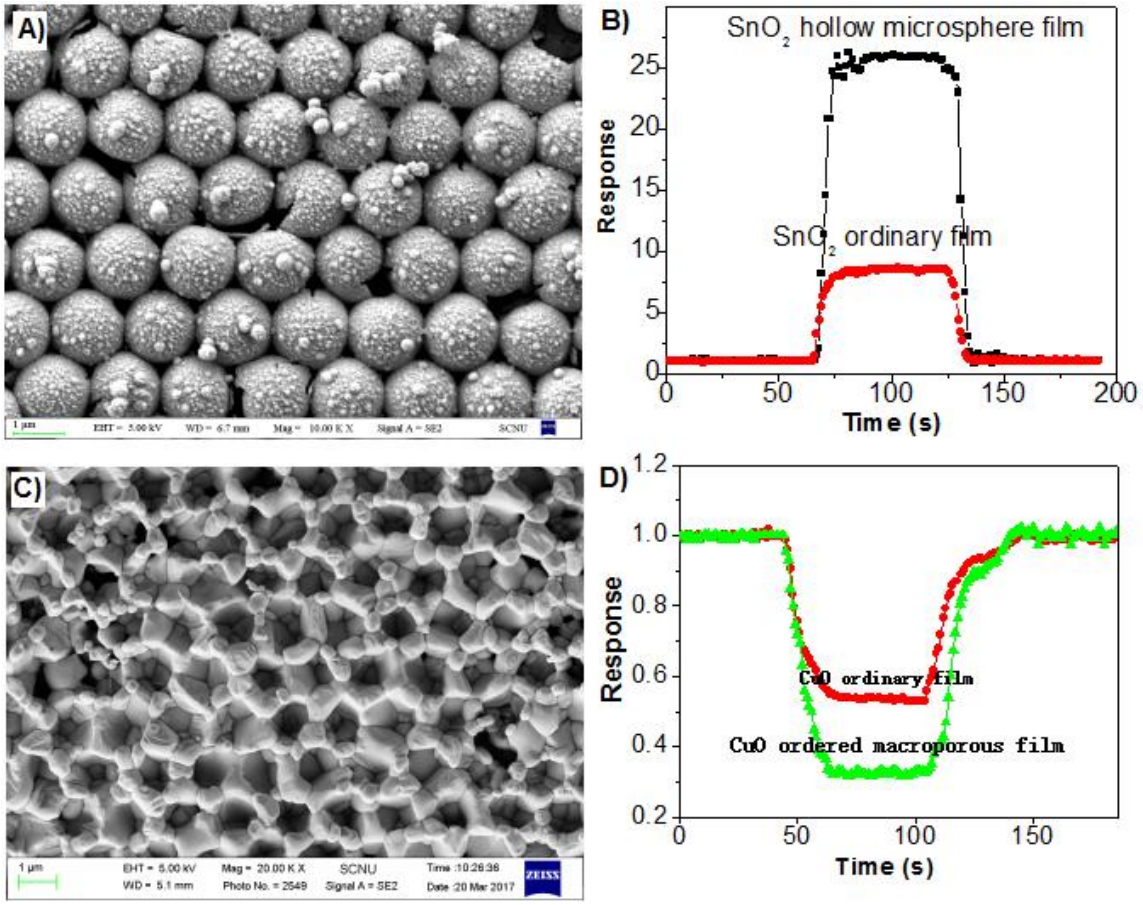

Fig. S11 SEM images of SnO_2 hollow microsphere film sensor (A) and CuO ordered macroporous film sensor (C), and their corresponding sensing responses to 50 ppm ethanol gas (B) and (D). The preparation conditions of the ordinary films are the same as the corresponding structural films, except for the absence of templates and / or surfactants during electrodeposition.

References -S

1 Y. V. Kaneti, Z. J. Zhang, J. Yue, Q. M. D. Zakaria, C. Y. Chen, X. C. Jiang, A. B. Yu, *Phys. Chem. Chem. Phys.,* 2014,**16**, 11471-11480.

2 M. R. Alenezi, A. S. Alshammari, K. D. G. I. Jayawardena, M. J. Beliatis, S. J. Henley, S. R. P. Silva, *J. Phys. Chem. C*, 2013, **117**, 17850-17858.

3 P. T. Hsieh, Y. C. Chen, K. S. Kao, C. M. Wang, *Appl. Phys. A: Mater. Sci. Process*, 2008, **90**, 317-321.

4 Y. Zhang, X.L. He, J.P. Li, Z.J. Miao, F. Huang, *Sensor. Actuat. B-Chem.*, 2008,**132**, 67-73.

5 P. Q. Hu, G. J. Du, W. J. Zhou, J. J. Cui, J. J. Lin, H. Liu, D. Liu, J. Y. Wang, S. W. Chen, *ACS Appl. Mater. Interfaces*, 2010, **2**, 3263-3269.

6 X. F. Chu, C. H. Wang, D. L. Jiang, C. M. Zheng, *Chem. Phys. Lett.*, 2004, **399**, 461-464.

7 R.S. Khadayate, R.B. Waghulde, M.G. Wankhede, J.V. Sali, P.P. Patil, *Bull. Mater. Sci.*, 2007, **30**, 129-133.

8 A. Mirzaei, K. Janghorban, B. Hashemi, M. Bonyani, S.G. Leonardi, G. Neri, *Ceram. Int.*, 2016, **42**, 6136-6144.

9 P. Raksa, A. Gardchareon, T. Chairuangsri, P. Mangkorntong, N. Mangkorntong, S. Choopun, *Ceram Int*, 2009, **35**, 649-652.

10 N. G. Cho, H. S. Woo, J. H. Lee, I. D. Kim, *Chem. Commun.*, 2011, **47**, 11300-11302.

11 Q. Z. Jiao, M. Fu, C. You, Y. Zhao, H. S. Li, *Inorg Chem.*, 2012, **51**, 11513-11520.

12 Z. J. Yin, Z. P. Sun, J. W. Wu, R. T. Liu, S. Y. Zhang, Y. N. Qian, Y. G. Min, *Appl Surf Sci*, 2018, **457**, 1103-1109.

13 Y. Zeng, T. Zhang, H. T. Fan, W. Y. Fu, G. Y. Lu, Y. M. Sui, H. B. Yang, *J. Phys. Chem. C,*

2009, **113**, 19000-19004.

14 N. Kaur, D. Zappa, M. Ferroni, N. Poli, M. Campanini, R. Negrea, E. Comini, *Sensor. Actuat. B-Chem.*, 2018, **262**, 477-485.

15 C. Qin, Y. Wang, Y. X. Gong, Z. Y. Zhang, J. L. Cao, *J. Alloy. Compd.*, 2019, **770,** 972-980.

16 Y. C. Xia, C. S. Wu, N. Y. Zhao, H. Zhang, *Mater Lett*, 2016, **171**, 117-120.